Angewandte Chemie International Edition

Angewandte International Edition Chemie

How to cite: *Angew. Chem. Int. Ed.* **2026**, e4052926
doi.org/10.1002/anie.4052926

RESEARCH ARTICLE Hot Paper

Imide Cyclophane Assemblies Enable Aquaporin-Like Water Transport

Yingxue Xu[1] | Hongshen Lin[1] | Linfeng Chen[2] | Wenju Chang[1] | Lipeng He[3] | Jie Shen[1] | Fan Xia[2] | Huaqiang Zeng[1]

[1]Fujian Provincial Key Laboratory of Molecular Synthesis and Functional Discovery, College of Chemistry, Fuzhou University, Fuzhou, China | [2]State Key Laboratory of Geomicrobiology and Environmental Changes, Engineering Research Center of Nano-Geomaterials of Ministry of Education, Faculty of Materials Science and Chemistry, China University of Geosciences, Wuhan, China | [3]College of Chemistry and Chemical Engineering, Lanzhou University, Lanzhou, China

Correspondence: Huaqiang Zeng (hqzeng@fzu.edu.cn)

Received: 9 May 2026 | **Revised:** 22 July 2026 | **Accepted:** 29 July 2026

Keywords: artificial water channels | cyclophane macrocycles | proton rejection | salt rejection | selective transport

ABSTRACT

Artificial water channels (AWCs) that replicate the high efficiency and selectivity of natural aquaporins are of considerable interest for desalination, water purification, and biomedical applications, yet the simultaneous realization of high permeability and perfect selectivity remains challenging. Herein, we report a class of self-assembled AWCs based on an imide cyclophane. Single-crystal analysis reveals that macrocycle **1** features an internal cavity of 3.5 Å × 6.3 Å, with a narrow constriction closely matching the dimensions of the selectivity filter of aquaporin 1. The assembled channel $(\mathbf{1})_4$ exhibits a single-channel water transport rate of up to 3.9×10^9 $H_2O\,s^{-1}$, corresponding to approximately 36% of AQP1 and representing one of the best-performing small-molecule self-assembled AWCs reported to date. Notably, it completely excludes NaCl, KCl, and protons. This work demonstrates that both the key structural feature and function of aquaporins can be emulated through a bottom-up supramolecular approach, providing a platform for the design of high-performance biomimetic membranes and channel-based therapeutics.

1 | Introduction

The discovery of aquaporins has revealed how biological systems achieve highly efficient and selective transmembrane water transport [1–5]. These integral membrane proteins enable ultrafast water permeation (10^9–10^{10} H_2O/s per channel) while completely excluding ions, including protons. Structural studies show that the selectivity filter of aquaporin-1 (AQP1), formed by cationic arginine and histidine residues, features a narrow constriction of ~3 Å, closely matching the kinetic diameter of a water molecule (~2.8 Å). This precise size exclusion, together with electrostatic and hydrophobic effects, effectively prevents the passage of ions [3]. With a permeability of $\sim 1.1 \times 10^{10}$ H_2O/s per channel, AQP1 exemplifies the rare combination of high flux and near-perfect selectivity.

Such performance underpins diverse physiological processes [6–9], from urinary concentration in the kidney to the regulation of brain edema, and dysfunction of aquaporins is implicated in diseases ranging from congestive heart failure to traumatic brain injury. Beyond biology, aquaporins provide a blueprint for addressing key technological challenges. In membrane-based desalination—a critical approach to mitigating global water scarcity—the trade-off between water permeability and salt rejection remains a central limitation [10–15], while in channelopathy research, there is an increasing need for molecular tools capable of precisely controlling water transport across membranes [6–9].

Inspired by nature, the construction of artificial water channels has emerged as a frontier in supramolecular chemistry [16–23],

aiming to develop functional materials for desalination, water purification, and the treatment of channelopathies. A variety of strategies have been explored, including imidazole quartets [14, 24, 25], hexa(*m*-phenylene ethynylene) macrocycles [26], pillararenes [27–31], aquafoldamers [32–36], porous organic cages [37], oligoureas [38], hydroxy channels [39, 40], alkylureido-trianglamines [41], self-assembled hydrazide channel [42], aramid foldamer [43], metal-directed β-helical tubules [44], pyridine-imidazole [45], and acylhydrazone-imidazole [46].

Notably, several polymer-based AWCs [33–36] have already surpassed the water transport rate of AQP1, while maintaining high rejection performance. More specifically, the best-performing AWC exhibits not only ~2.5-fold as high permeability as AQP1 but also efficiently excludes salts and protons [34]. In contrast, AWCs assembled from small molecules or macrocycles still lag substantially behind their biological counterparts. Except for three notable examples exhibiting water permeation rates of 2.7–3.0 × 10^9 H_2O/s per channel [28, 32, 37], most reported systems display water fluxes in the range of 10^6–10^8 H_2O/s [14, 24–27, 29–31, 38–46], remaining significantly lower than those of natural aquaporins (10^9–10^{10} H_2O/s).

Imide macrocycles, such as those based on pyromellitic diimide (PMDI) and naphthalene diimide (NDI), feature rigid, electron-deficient aromatic cores [47–50]. Their cavity dimensions can be precisely tuned by varying the length and configuration of the bridging linkers. These macrocycles are readily accessible via condensation between aromatic dianhydrides and diamines and have found broad applications in host–guest chemistry, energy storage, optoelectronics, and adsorption/separation. Nevertheless, their potential as building blocks for high-performance AWCs remains unexplored.

Herein, we report an AWC system based on the self-assembly of a rigid imide tetramer macrocycle. The system is constructed from a [2+2] cyclophane derived from pyromellitic diimide and *p*-xylylene linkers, without any side-chain modifications (Figure 1a). The resulting molecule features a cylindrical cavity measuring 3.5 Å × 6.3 Å (Figure 1b), with the short dimension of 3.5 Å closely matching the diameter of a water molecule and the 2.2 Å × 2.6 Å dimensions of the AQP1 selectivity filter (Figure 1c) [3]. Leveraging its intrinsic backbone rigidity and H-bonding sites, four macrocycles self-assemble via intermolecular H-bonding to form a transmembrane channel with a height of 3.1 nm. This channel exhibits a single-channel water transport rate of up to 3.9 × 10^9 H_2O/s per channel, equivalent to ~36% of AQP1's permeability, while completely rejecting salts and protons, thereby integrating high flux with high selectivity. It thus ranks among the best-performing small-molecule self-assembled AWCs reported to date [14, 24–32, 37–46].

1.1 | Molecular Design and Synthesis

Macrocycle **1**, a [2+2] cyclophane constructed from pyromellitic diimide bridged by *p*-xylylene groups, was obtained in 33% overall yield via a three-step synthesis (Figure 1a). DFT molecular modeling [51] indicates that **1** possesses a cylindrical internal cavity with approximate dimensions of 3.4 Å × 6.5 Å (Figure S1). Critically, the calculated 3.4 Å in width closely approximates the kinetic diameter of water (~2.8 Å) and the constriction size of the native AQP1 selectivity filter (2.2 Å × 2.6 Å, Figure 1c) [3]. This precise dimensional matching provides a key structural basis for high ion selectivity, as fully hydrated ions with their complete van der Waals shells (e.g., ~7.5-10.1 Å for $[Na(H_2O)_6]^+$ and ~9.0–9.6 Å for $[K(H_2O)_6]^+$) [36] would be sterically excluded. Moreover, the absence of peripheral side chains in this system minimizes steric hindrance during self-assembly, while the carbonyl O-atoms of the imide groups are positioned to act as H-bond acceptors, potentially interacting with aromatic C–H groups of adjacent macrocycles to drive an ordered intermolecular arrangement in a bilayer membrane.

To obtain atomic structural information and validate this design, single crystals of macrocycle **1** were grown and analyzed by x-ray crystallography (Table S1). The crystal structure (Figure 1b) reveals a rectangle-shaped internal cavity of 3.5 Å × 6.3 Å for **1**, in excellent agreement with the DFT-calculated structure. Further analysis shows that adjacent molecules stack via H-bonding interactions (2.1–2.8 Å, Figure 1b) between imide carbonyl O-atoms and aromatic C–H groups, with four molecules of **1** assembling into a transmembrane channel, $(\mathbf{1})_4$, with a height of 3.1 nm (Figure 1b). Notably, in the crystal structure, one *p*-xylylene unit rotates by 90° to accommodate a DMSO molecule. Nevertheless, under membrane-mimetic aqueous conditions, molecular dynamics simulations [52] in a DOPC lipid bilayer reveal that DMSO-free molecules of **1** stacks in a regular fashion, with the rotated *p*-xylylene unit rotating back to adopt a parallel conformation relative to its opposing *p*-xylylene unit (Figures 1e and S2a). This discrepancy indicates that guest inclusion within an individual macrocycle cavity in the solid state does not necessarily reflect the structural organization of the assembled channel in a membrane environment. MD simulations further confirm the stability of the H-bonded assembly $(\mathbf{1})_4$ within the membrane, demonstrating its ability to effectively span the hydrophobic membrane core (Figure 1d) and form a narrow hydrophobic cavity of 3.1 Å × 6.8 Å (Figure 1e).

Analysis of the simulated water distribution within the cavity of $(\mathbf{1})_4$ (approx. 3.1 Å × 6.8 Å) reveals three distinct types of water molecules (Figure 1e): type 1 species are tetrahedrally H-bonded to four neighboring water molecules; type 2 engage in two H-bonds with adjacent water molecules and additionally form O—H···π interactions with the benzene rings; and type 3 are coordinated via two H-bonds to neighboring water molecules and one H-bond to a carbonyl oxygen atom of the channel wall. On this basis, the ultrafast water permeation through $(\mathbf{1})_4$ is attributed to a synergistic interplay of water–water H-bonding and the low-friction environment provided by the aromatic channel surfaces. This mechanistic scenario resembles that of the water-conduction pathway in AQP1, which features a narrow selectivity filter (2.2 Å × 2.6 Å, Figure 1c) where intermolecular H-bonds operate along one side of the pore while hydrophobic residues on the opposite wall reduce frictional resistance [53]. In contrast to the single-file transport mode characteristic of AQP1, however, the lumen of $(\mathbf{1})_4$ accommodates multiple confined water molecules, pointing toward a multi-water transport mechanism.

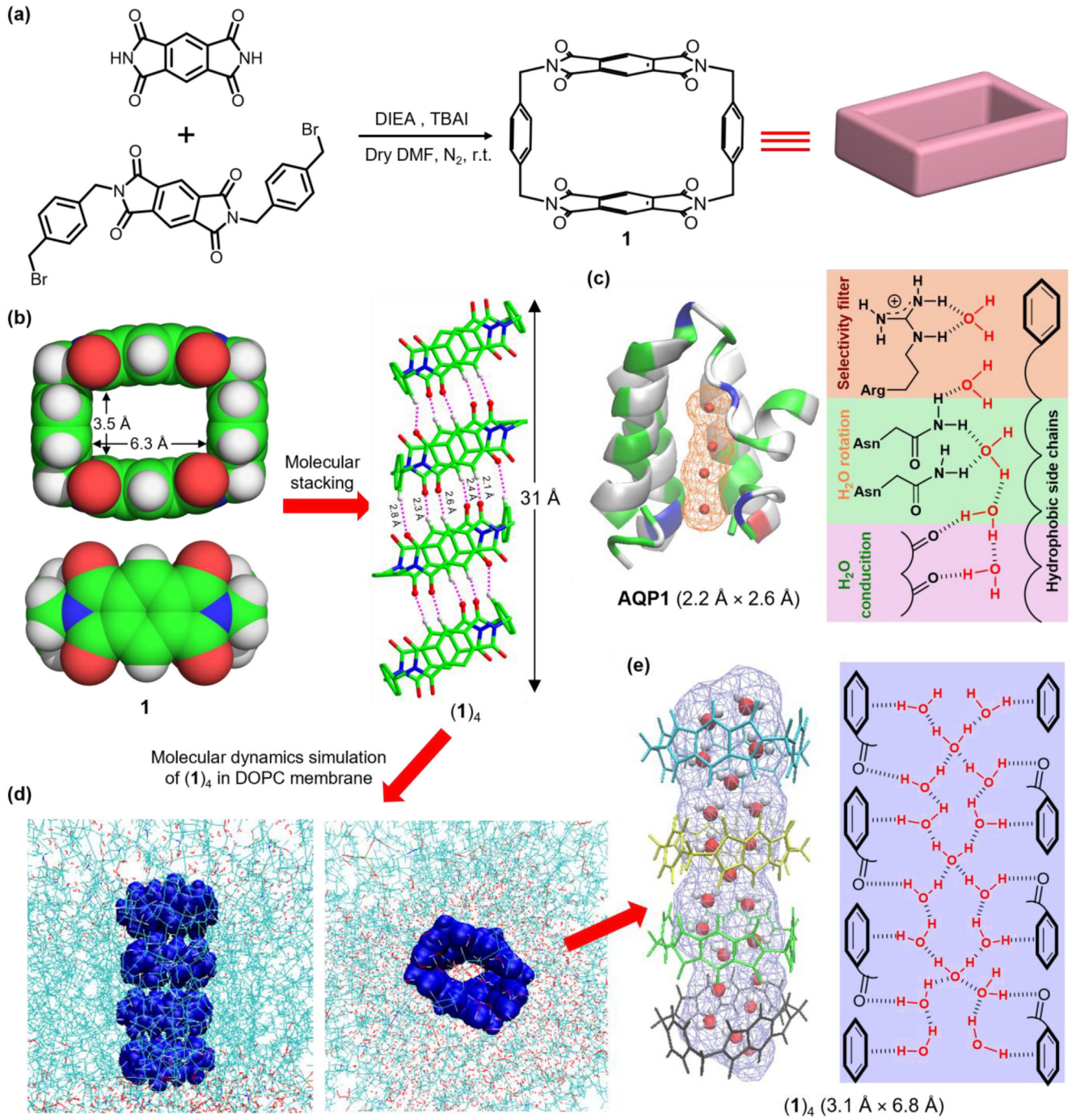

FIGURE 1 | (a) Molecular design and synthetic construction of imide cyclophane **1**. (b) Top and side views of the crystal structure of 1 (CCDC No. 2540875), revealing a rectangular cavity of 3.5 × 6.3 Å, together with the H-bonded dimeric $(\mathbf{1})_2$ and tetrameric $(\mathbf{1})_4$ assemblies exhibiting an overall height of 3.1 nm. Color code: O, red; H, white; C, green; N, blue. (c) One-dimensional stacking of $(\mathbf{1})_4$ generates a membrane-spanning hollow cavity of sufficient dimensions to accommodate H_2O transport. (d) Distinct water-transport modes of AQP1 and $(\mathbf{1})_4$. AQP1 transports water through a narrow polar single-file pathway (~2.2 × 2.6 Å), whereas membrane-embedded $(\mathbf{1})_4$ provides a wider confined lumen (~3.1 × 6.8 Å) that accommodates multiple confined water molecules.

1.2 | High Water Permeability of 1

Single-channel water permeability (P_{sc} in cm^3/s) was investigated using a stopped-flow method with 0.3 M sucrose as the draw solution (Figure 2a) [32–36]. By varying the lipid-to-channel molar ratio (mLCR) from 400:1 to 8000:1, channel $(\mathbf{1})_4$ achieves maximal permeability at an mLCR of 6000:1 (Figure 2b). This optimum arises from a confluence of factors, including changes in membrane incorporation efficiency, vesicle dimensions, background vesicle leakiness, denser packing of channel-embedded vesicles, and the orientation of the inserted channels. It should be noted that blank DOPC vesicles possess intrinsic osmotic

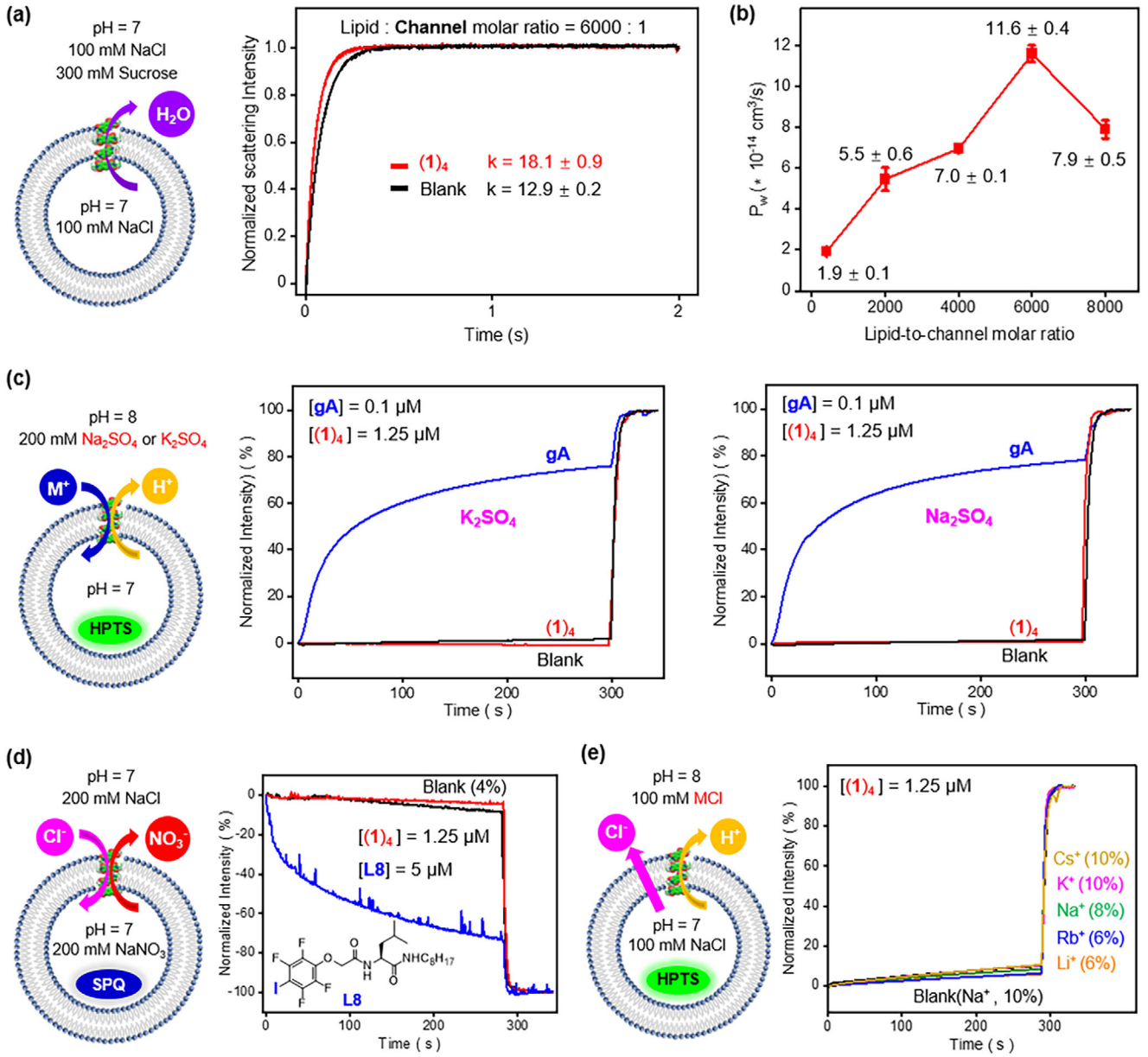

FIGURE 2 | High water permeability of AWC $(\mathbf{1})_4$ with excellent salt and proton rejection properties. (a) Schematic illustration of the LUV-based water permeability assay, in which a 300 mM sucrose solution was used to establish an inward osmotic gradient for recording stopped-flow light-scattering traces of blank DOPC LUVs and LUVs reconstituted with $(\mathbf{1})_4$. (b) Water permeability measurements of channel $(\mathbf{1})_4$ at varying lipid-to-channel molar ratios. Data in (a) and (b) are shown as mean ± SD from three independent experiments ($n = 3$). (c) HPTS-based LUV assays performed under high ion concentration gradients, confirming that $(\mathbf{1})_4$ does not transport Na^+ or K^+ ions. (d) Chloride-sensitive SPQ assays, demonstrating the absence of anion transport by $(\mathbf{1})_4$ and high anion transport by well-established anion channel **L8** [54]. (e) HPTS-based LUV assays under a transmembrane proton gradient, establishing the inability of $(\mathbf{1})_4$ to mediate proton transport. HPTS = 8-hydroxypyrene-1,3,6-trisulfonic acid; SPQ = 6-methoxy-*N*-(3-sulfopropyl)quinolinium.

water permeability, which contributes substantially to the overall stopped-flow light-scattering response. Therefore, the water transport activity of the channel was evaluated based on the reproducible enhancement in osmotic water permeability relative to blank DOPC vesicles, rather than on the absolute scattering intensity change alone. At the optimal lipid-to-channel molar ratio of 6000:1, presence of the water channel increased the exponential coefficient from 12.9 ± 0.2 for blank DOPC vesicles to 18.1 ± 0.9 for channel-containing vesicles, giving rise to the calculated P_f values of 0.011919 and 0.016972 cm/s, respectively. The single-channel permeability was calculated from the channel-specific permeability contribution after subtraction of the intrinsic lipid background, affording a P_{sc} value of $(11.6 \pm 0.4) \times 10^{-14}$ cm^3/s at the optimal lipid-to-channel molar ratio of 6000:1 (Figure 2b).

However, owing to fluorescence quenching of $(\mathbf{1})_4$ in the phospholipid membrane (Figure S7) [54], the actual channel insertion efficiencies could not be directly determined. Considering that the extrusion process leads to an approximately 57% loss of phospholipids (Figure S6), and that the extrusion loss of $(\mathbf{1})_4$

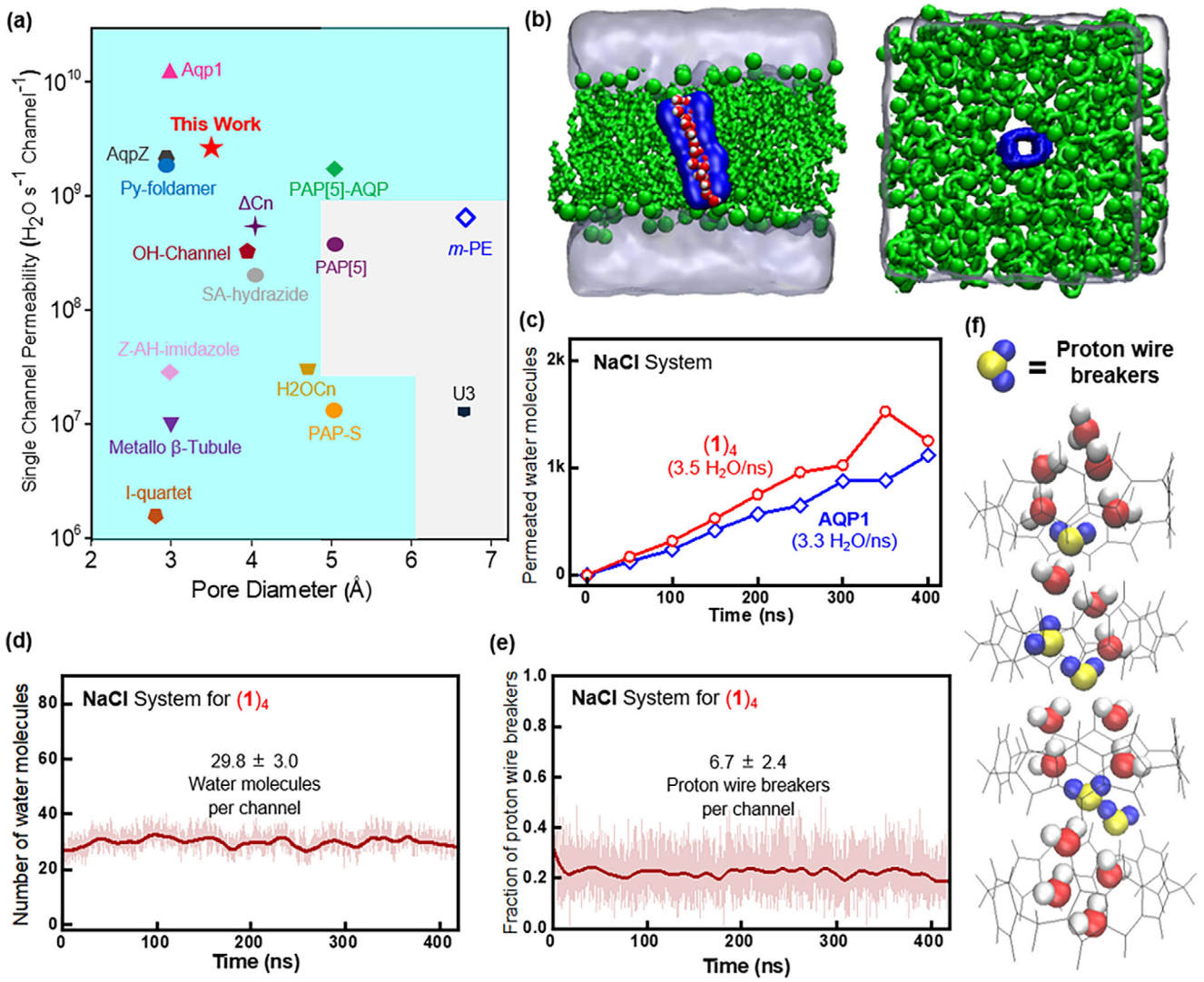

FIGURE 3 | (a) Comparison of natural aquaporins (AqpZ [4] and AQP1 [3]) with self-assembled artificial water channels constructed from small molecules, including Py-foldamer [32], PAP [5]-AQP [28], m-PE [24], ΔCn [41], PAP [5] [27], OH-channel [39], SA-hydrazide [42], Z-AH-imidazole [46], H_2OCn [38], PAP-S [31], U3 [45], Metallo *β*-Tubule [44], and I-quartet [26]). Systems located in the light blue-shaded region exhibit salt-rejection capability, whereas those in the grey region are ion-conductive. (b) Representative MD snapshot of water-filled $(\mathbf{1})_4$ of 3.1 nm in height, embedded within a DOPC lipid bilayer. (c) MD-derived water transport rates of $(\mathbf{1})_4$ and AQP1 in a NaCl-containing system. (d) Number of water molecules residing inside the channel, with an average occupancy of 29.8 water molecules. (e) Number of water molecules acting as proton-wire breakers within the channel, with an average fraction of 23% (6.7 breakers per channel). (f) Representative water cluster composed of 21 water molecules, 5 of which function as proton wire breakers, thereby suppressing proton translocation through the Grotthuss mechanism.

is positively correlated with its water transport activity, a conservative estimate assuming a channel loss of 0%–57% yields a single-channel permeability in the range of 5.0×10^{-14} cm^3/s to 11.6×10^{-14} cm^3/s for $(\mathbf{1})_4$. This corresponds to water transport rates of 1.7×10^9 to 3.9×10^9 H_2O/s per channel, which is approximately 15%–36% of the transport rate of AQP1 [3] and places $(\mathbf{1})_4$ among the highest-performing small-molecule self-assembled artificial water channels reported to date (Figure 3a) [14, 24–32, 37–46].

To exclude the possibility that the enhanced water permeability arises from nonspecific membrane disruption, a carboxyfluorescein (CF) leakage assay was performed using CF-encapsulated DOPC vesicles (Figure S8). Upon addition of $(\mathbf{1})_4$ at 1.25 μM, negligible CF release was observed, which is comparable to that of blank DOPC vesicles, indicating that $(\mathbf{1})_4$ does not compromise membrane integrity. In contrast, the pore-forming peptide melittin induces pronounced CF leakage, resulting in leakage efficiencies of 34.5% and 89.7% at 50 and 100 nM, respectively. These results demonstrate that the water transport activity of $(\mathbf{1})_4$ is unlikely to originate from nonspecific membrane defects, but rather from selective channel-mediated transport.

The activation energy for water transport through $(\mathbf{1})_4$ was determined from temperature-dependent stopped-flow measurements after subtraction of the DOPC background contribution (Figure S9). The analysis affords activation energies of 17.8 ± 0.8 kcal mol^{-1} for $(\mathbf{1})_4$ and 12.7 ± 0.2 kcal mol^{-1} for blank DOPC vesicles. We note that the apparent activation energy of $(\mathbf{1})_4$ is higher than that of blank DOPC vesicles and also higher than

the value reported for AQP1 (ca. 5 kcal mol^{-1}) [3]. At present, we cannot unambiguously assign the molecular origin of this difference. However, literature precedents indicate that activation energy does not necessarily scale directly with the absolute water permeation rate. For instance, two artificial water channels with a 15-fold difference in single-channel water permeation rate (3.0×10^9 vs. 0.2×10^9 H_2O/s per channel) exhibit nearly identical activation energies (12.06 ± 0.31 vs. 12.25 ± 0.25 kcal mol^{-1}) [32].

1.3 | High Rejection of Salts and Protons by 1

A critical requirement for an ideal AWC is the efficient rejection of salts, particularly NaCl, KCl, and even protons. The exclusion of Na^+ and K^+ cations was further evaluated using fluorescence-based assays with the pH-sensitive dye HPTS encapsulated in large unilamellar vesicles (LUVs, Figure 2c). In this assay, the intravesicular pH was maintained at 7, while the extravesicular solution was adjusted to pH 8 in the presence of 200 mM M_2SO_4 (M = Na or K). Under these conditions, a transmembrane salt gradient drives H^+/M^+ antiport, resulting in an increase in the intravesicular pH and a corresponding enhancement in HPTS fluorescence. At 1.25 μM, $(\mathbf{1})_4$ shows no detectable response to either Na^+ or K^+ gradients, indicating negligible cation transport activity. In contrast, gramicidin A (gA) at 0.1 μM efficiently transported both Na^+ (78%) and K^+ (76%) cations, as evidenced by pronounced fluorescence increases (Figure 2c). These results confirm that **1** effectively excludes alkali metal cations while maintaining selective water permeability without accompanying ion transport.

The anion transport capability of AWC $(\mathbf{1})_4$ was assessed using a Cl^--sensitive SPQ fluorescence assay (Figure 2d). As expected, $(\mathbf{1})_4$ at 1.25 μM induces minimal SPQ fluorescence quenching relative to the blank control, indicating negligible Cl^- transport activity. In contrast, the well-established Cl^- transporter **L8** [55], tested at the same concentration, caused a pronounced decrease (73%) in SPQ fluorescence intensity, consistent with substantial Cl^- transport. These results further highlight the high selectivity of $(\mathbf{1})_4$, demonstrating its ability to effectively exclude not only cations but also anions such as Cl^-.

To evaluate proton translocation, a transmembrane pH gradient was established across the lipid membrane (Figure 2e). Specifically, the intravesicular compartment of the LUVs contained 100 mM NaCl at pH 7, while the extravesicular solution was adjusted to pH 8 with 100 mM MCl (M = Li, Na, K, Rb, or Cs). If $(\mathbf{1})_4$ were capable of proton transport, proton efflux accompanied by passive Cl^- diffusion to maintain charge neutrality would increase the intravesicular pH, resulting in enhanced fluorescence of the encapsulated HPTS dye. However, compared with the corresponding blank controls (Figure S3), no appreciable fluorescence enhancement was observed upon addition of **1** (5 μM) in any of the five alkali metal chloride buffers, indicating negligible proton transport activity.

To further quantify proton permeability, a conservative estimation method was employed (see "Estimation of Proton Transport Rate" and Figure S10 in the Supporting Information for details), yielding an estimated proton transport rate of less than for $(\mathbf{1})_4$. This corresponds to a water-to-proton selectivity ratio of 1.6×10^{11} to 3.9×10^{11}, highlighting the extreme selectivity of **1** for water transport over protons.

1.4 | MD-Simulated Water Transport Property of 1

Analysis of reported self-assembled AWCs formed by small molecules reveals that the simultaneous achievement of high water permeability and aquaporin-like salt rejection remains rare (Figure 3a) [14, 24–32, 37–46]. With the exception of three previously reported systems [28, 32, 37] exhibiting water transport rates on the order of 10^9 H_2O/s per channel, all other small moelcule-based AWCs display water fluxes ranging from 10^6 to 10^8 H_2O/s per channel, substantially lower than those of natural aquaporins such as AqpZ (~10^9 H_2O/s per channel) and AQP1 (~10^{10} H_2O/s per channel). In this context, $(\mathbf{1})_4$, with water transport rates up to 3.9×10^9 H_2O/s per channel, represents one of the highest-performing small-molecule-based artificial water channel reported to date.

To gain computational insight into the water permeability and selectivity of $(\mathbf{1})_4$ relative to AQP1, all-atom molecular dynamics (MD) simulations were performed in a NACl environment over a 400 ns trajectory [56]. The root-mean-square deviation (RMSD) values converged to ~0.27 nm within approximately 10 ns (Figure S11), indicating equilibration of the system. Throughout the subsequent simulation period, $(\mathbf{1})_4$ a stable equilibrium conformation within the DOPC membrane under 0.6 M NaCl conditions (Figure 3b). The simulation system comprised 4736 water molecules and 48 NaCl pairs. Over the 400 ns trajectory, $(\mathbf{1})_4$ facilitates the transport of 1249 water molecules, corresponding to a flux of 3.5×10^9 H_2O/s per channel (Figure 3c and Supporting Movies S1). In addition, the simulated water conduction rate of 1.9×10^9 H_2O/s per channel for $(\mathbf{1})_3$ is substantially lower than the experimentally determined value of 3.9×10^9 H_2O/s per channel for **1**. Together with the SAXS (small-angle x-ray scattering) data discussed below, this discrepancy indicates that $(\mathbf{1})_4$, rather than $(\mathbf{1})_3$, is the primary channel structure responsible for water transport. In comparison, AQP1 exhibits a computed water transport rate of 3.3×10^9 H_2O/s per channel. Additionally, 37 833 water molecules penetrated at least ~2 Å into $(\mathbf{1})_4$ (corresponding to approximately 1/16 of the channel length), whereas no Na^+ or Cl^- ions were observed to traverse the channel throughout the simulation. Based on these data, the estimated water-to-NaCl selectivity ratio is at least 383, calculated as 37 833/(4736/48).

These MD simulations demonstrate that the water transport efficiency of $(\mathbf{1})_4$ is comparable to that of AQP1, while exhibiting exceptional selectivity against Na^+ and Cl^- ions, in excellent agreement with the experimental observations. Collectively, these findings establish $(\mathbf{1})_4$ as a highly efficient and selective artificial water channel with performance approaching that of natural aquaporins.

1.5 | Proton Wire Breakers to Block Proton Transport

Despite the substantial population of water molecules within the lumen of $(\mathbf{1})_4$ (Figure 3b,d), experimental results indicate that

these confined waters do not readily support proton transport. At any given time, approximately 20–40 water molecules occupy the channel interior, with an average lumen occupancy of 29.8 water molecules (Figure 3d). Among them, ~23% of the confined water molecules, corresponding to an average of 6.7 water molecules per channel (Figure 3e), function as "proton wire breakers" (Figure 3f) [35]. These water molecules interact with neighboring waters through either zero or a single hydrogen bond, or through two hydrogen bonds exclusively via either O-atoms or H-atoms (Figure 3f). Such configurations disrupt the continuity of the H-bonded water network across the channel, thereby suppressing proton translocation through the Grotthuss hopping mechanism. Notably, a similar proton-breaking water motif, in which a water molecule forms two hydrogen bonds exclusively through its H atoms, is also observed in the NPA motif of aquaporins [57].

1.6 | SAXS-Derived Aggregation Models of $(\mathbf{1})_4$

To obtain possible aggregation models of **1** in DOPC-membrane (Figure S12a), SAXS measurements were performed on dry DOPC/**1** mixed powder samples prepared by co-dissolving DOPC and **1** in chloroform at a DOPC:**1** molar ratio of 1500:1, followed by solvent removal. A DOPC-only sample prepared under the same conditions was used as the control. Compared with the blank DOPC sample, the DOPC/**1** sample displays additional fingerprint scattering peaks at 30.6, 19.6, 9.6, and 7.2 Å (Figure S12b). These peaks are in reasonable agreement with the simulated SAXS spectra for the crystal structure-derived $(\mathbf{1})_4$-based two-dimensional stacking models, with widths of 4–7 nm and lengths of 4.6–7.9 nm (Figure S12b–d). We therefore propose that nanometer-sized finite lateral assemblies of $(\mathbf{1})_4$ columns may contribute to the ion transport activities (for further details, see the discussion in the Supporting Information).

2 | Summary

In summary, we report an artificial water channel derived from the self-assembly of a pyromellitic diimide-based macrocycle **1**, which successfully mimics both the key structural feature and function of natural aquaporins through a bottom-up supramolecular strategy. The rigid macrocycles assemble through intermolecular H-bonding interactions to form a stacked transmembrane channel with an overall height of 3.1 nm. Each macrocycle contains an intrinsic cavity of 6.3 Å × 3.5 Å, and the narrow constriction generated upon assembly closely resembles the dimensions of the native AQP1 selectivity filter, thereby providing a structural basis for efficient ion exclusion. Functionally, the channel achieves a high single-channel water transport rate of 3.9×10^9 H_2O/s, reaching 36% of the transport efficiency of AQP1, while simultaneously exhibiting complete rejection of NaCl, KCl, and protons. To the best of our knowledge, it represents one of the best-performing artificial water channels constructed through small-molecule self-assembly reported to date. This work establishes a new supramolecular platform for biomimetic separation membranes with potential applications in large-scale desalination and water purification. Future studies will focus on modulating lumen hydrophilicity to further enhance water permeability, as well as exploring biomedical applications, including membrane repair materials and therapies targeting channelopathies.

Author Contributions

Yingxue Xu: data curation, methodology, investigation, writing – original draft, formal analysis. **Hongshen Lin:** investigation. **Linfeng Chen:** funding acquisition, investigation. **Wenju Chang:** software, formal analysis. **Lipeng He:** software, data curation. **Jie Shen:** writing – original draft, writing – review and editing, investigation, methodology, data curation, supervision, formal analysis, funding acquisition. **Fan Xia:** project administration, supervision, funding acquisition, investigation. **Huaqiang Zeng:** conceptualization, project administration, funding acquisition, writing – review and editing, resources, supervision, formal analysis.

Acknowledgments

We greatly appreciate the support of this work by the National Key R&D Program of China (2021YFA1200403), the National Natural Science Foundation of China (22271049 and 22371048), the "Chu ying Program" for the Top Young Talents of Fujian Province, the Natural Science Foundation of Fujian Province (2023J01054), and a start-up grant from Fuzhou University.

Conflicts of Interest

The authors declare no conflicts of interest.

Data Availability Statement

The data that support the findings of this study are available from the corresponding author upon reasonable request.

References

1. K. Murata, K. Mitsuoka, T. Hirai, et al., "Structural Determinants of Water Permeation Through Aquaporin-1," *Nature* 407 (2000): 599–605, https://doi.org/10.1038/35036519.

2. P. Agre, "The Aquaporin Water Channels," *Proceedings of the American Thoracic Society* 3 (2006): 5–13, https://doi.org/10.1513/pats.200510-109JH.

3. A. Horner, F. Zocher, J. Preiner, et al., "The Mobility of Single-File Water Molecules is Governed by the Number of H-bonds They May Form With Channel-lining Residues," *Science Advances* 1 (2015): e1400083, https://doi.org/10.1126/sciadv.1400083.

4. A. Horner, C. Siligan, A. Cornean, and P. Pohl, "Positively Charged Residues at the Channel Mouth Boost Single-File Water Flow," *Faraday Discussions* 209 (2018): 55–65, https://doi.org/10.1039/C8FD00050F.

5. J. E. Hall, J. A. Freites, and D. J. Tobias, "Experimental and Simulation Studies of Aquaporin 0 Water Permeability and Regulation," *Chemical Reviews* 119 (2019): 6015–6039, https://doi.org/10.1021/acs.chemrev.9b00106.

6. A. S. Verkman, "Aquaporins," *Current Biology* 23 (2013): R52–R55, https://doi.org/10.1016/j.cub.2012.11.025.

7. W. B. Bollag, L. Aitkens, J. White, and K. A. Hyndman, "Aquaporin-3 in the Epidermis: More Than Skin Deep," *American Journal of Physiology-Cell Physiology* 318 (2020): C1144–C1153, https://doi.org/10.1152/ajpcell.00075.2020.

8. F. H. Login and L. N. Nejsum, "Aquaporin Water Channels: Roles Beyond Renal Water Handling," *Nature Reviews Nephrology* 19 (2023): 604–618, https://doi.org/10.1038/s41581-023-00734-9.

9. C. S. Vrettou, V. Issaris, S. Kokkoris, et al., "Exploring Aquaporins in Human Studies: Mechanisms and Therapeutic Potential in Critical Illness," *Life* 14 (2024): 1688, https://doi.org/10.3390/life14121688.

10. J. R. Werber, C. O. Osuji, and M. Elimelech, "Materials for Next-Generation Desalination and Water Purification Membranes," *Nature Reviews Materials* 1 (2016): 16018, https://doi.org/10.1038/natrevmats.2016.18.

11. W. Song and M. Kumar, "Artificial Water Channels: Toward and Beyond Desalination," *Current Opinion in Chemical Engineering* 25 (2019): 9–17, https://doi.org/10.1016/j.coche.2019.06.007.

12. R. Zhang, J. Tian, S. Gao, and B. Van der Bruggen, "How to Coordinate the Trade-Off Between Water Permeability and Salt Rejection in Nanofiltration?," *Journal of Materials Chemistry A* 8 (2020): 8831–8847, https://doi.org/10.1039/D0TA02510K.

13. H. Shemer, S. Wald, and R. Semiat, "Challenges and Solutions for Global Water Scarcity," *Membranes* 13 (2023): 612, https://doi.org/10.3390/membranes13060612.

14. M. Di Vincenzo, A. Tiraferri, V.-E. Musteata, et al., "Biomimetic Artificial Water Channel Membranes for Enhanced Desalination," *Nature Nanotechnology* 16 (2021): 190–196.

15. L.-B. Huang, M. Di Vincenzo, M. G. Ahunbay, et al., "Bilayer Versus Polymeric Artificial Water Channel Membranes: Structural Determinants for Enhanced Filtration Performances," *Journal of the American Chemical Society* 143 (2021): 14386–14393, https://doi.org/10.1021/jacs.1c07425.

16. W. Si, P. Xin, Z.-T. Li, and J.-L. Hou, "Tubular Unimolecular Transmembrane Channels: Construction Strategy and Transport Activities," *Accounts of Chemical Research* 48 (2015): 1612–1619, https://doi.org/10.1021/acs.accounts.5b00143.

17. Y. Huo and H. Zeng, ""Sticky"-Ends-Guided Creation of Functional Hollow Nanopores for Guest Encapsulation and Water Transport," *Accounts of Chemical Research* 49 (2016): 922–930, https://doi.org/10.1021/acs.accounts.6b00051.

18. B. Gong, "Artificial Water Channels: Inspiration, Progress, and Challenges," *Faraday Discussions* 209 (2018): 415–427, https://doi.org/10.1039/C8FD00132D.

19. Y. J. Lim, K. Goh, and R. Wang, "The Coming of Age of Water Channels for Separation Membranes: From Biological to Biomimetic to Synthetic," *Chemical Society Reviews* 51 (2022): 4537–4582, https://doi.org/10.1039/D1CS01061A.

20. W. Song and M. Kumar, "Beyond Aquaporins: Recent Developments in Artificial Water Channels," *Langmuir* 38 (2022): 9085–9091, https://doi.org/10.1021/acs.langmuir.2c01605.

21. Z. Qiu, J. Chen, J. Zeng, R. Dai, and Z. Wang, "A Review on Artificial Water Channels Incorporated Polyamide Membranes for Water Purification: Transport Mechanisms and Performance," *Water Research* 247 (2023): 120774, https://doi.org/10.1016/j.watres.2023.120774.

22. D.-D. Su and M. Barboiu, "Hydrogen-Bonded Water-Wires/Clusters–Toward Natural Selectivity of Artificial Water Channels," *Coordination Chemistry Reviews* 515 (2024): 215973, https://doi.org/10.1016/j.ccr.2024.215973.

23. D. Zhang, W. Chang, J. Shen, and H. Zeng, "Aromatic Foldamer-Derived Transmembrane Transporters," *Chemical Communications* 60 (2024): 13468–13491, https://doi.org/10.1039/D4CC04388J.

24. Y. Le Duc, M. Michau, A. Gilles, et al., "Imidazole-Quartet Water and Proton Dipolar Channels," *Angewandte Chemie International Edition* 50 (2011): 11366–11372.

25. E. Licsandru, I. Kocsis, Y.-X. Shen, et al., "Salt-Excluding Artificial Water Channels Exhibiting Enhanced Dipolar Water and Proton Translocation," *Journal of the American Chemical Society* 138 (2016): 5403–5409, https://doi.org/10.1021/jacs.6b01811.

26. X. Zhou, G. Liu, K. Yamato, et al., "Self-Assembling Subnanometer Pores With Unusual Mass-Transport Properties," *Nature Communications* 3 (2012): 949, https://doi.org/10.1038/ncomms1949.

27. Y.-X. Shen, W. Si, M. Erbakan, et al., "Highly Permeable Artificial Water Channels That Can Self-Assemble Into Two-Dimensional Arrays," *Proceedings National Academy of Science USA* 112 (2015): 9810–9815, https://doi.org/10.1073/pnas.1508575112.

28. Z.-J. Yan, D. Wang, Z. Ye, et al., "Artificial Aquaporin That Restores Wound Healing of Impaired Cells," *Journal of the American Chemical Society* 142 (2020): 15638–15643, https://doi.org/10.1021/jacs.0c00601.

29. I.-M. Andrei, D. Strilets, S. Fa, M. Baaden, T. Ogoshi, and M. Barboiu, "Combinatorial Screening of Water/Proton Permeation of Self-Assembled Pillar[5]Arene Artificial Water Channel Libraries," *Angewandte Chemie International Edition* 62 (2023): e202310812, https://doi.org/10.1002/anie.202310812.

30. Q. Xiao, T. Fan, Y. Wang, Z.-T. Li, J.-L. Hou, and Y. Wang, "Artificial Water Channel That Couples With Cell Protrusion Formation," *CCS Chem* 5 (2023): 1745–1752, https://doi.org/10.31635/ccschem.023.202302975.

31. I. M. Andrei, W. Chen, M. Baaden, S. P. Vincent, and M. Barboiu, "Proton-Versus Cation-Selective Transport of Saccharide Rim-Appended Pillar[5]Arene Artificial Water Channels," *Journal of the American Chemical Society* 145 (2023): 21904–21914, https://doi.org/10.1021/jacs.3c06335.

32. J. Shen, R. Ye, A. Romanies, et al., "Aquafoldmer-Based Aquaporin-Like Synthetic Water Channel," *Journal of the American Chemical Society* 142 (2020): 10050–10058, https://doi.org/10.1021/jacs.0c02013.

33. J. Shen, J. Fan, R. Ye, N. Li, Y. Mu, and H. Zeng, "Polypyridine-Based Helical Amide Foldamer Channels: Rapid Transport of Water and Protons With High Ion Rejection," *Angewandte Chemie International Edition* 59 (2020): 13328–13334, https://doi.org/10.1002/anie.202003512.

34. A. Roy, J. Shen, H. Joshi, et al., "Foldamer-Based Ultrapermeable and Highly Selective Artificial Water Channels That Exclude Protons," *Nature Nanotechnology* 16 (2021): 911–917, https://doi.org/10.1038/s41565-021-00915-2.

35. J. Shen, A. Roy, H. Joshi, et al., "Fluorofoldamer-Based Salt- and Proton-Rejecting Artificial Water Channels for Ultrafast Water Transport," *Nano Letters* 22 (2022): 4831–4838, https://doi.org/10.1021/acs.nanolett.2c01137.

36. J. Shen, Y. Zhang, Y. Jin, et al., "Butterfly-Shaped Folding Synthons for Designing Superselective and Ultrapermeable Artificial Water Channels," *Angewandte Chemie International Edition* 64 (2025): e202506341, https://doi.org/10.1002/anie.202506341.

37. Y. D. Yuan, J. Dong, J. Liu, et al., "Porous Organic Cages as Synthetic Water Channels," *Nature Communications* 11 (2020): 4927, https://doi.org/10.1038/s41467-020-18639-7.

38. C. Dutta, P. Krishnamurthy, D. Su, et al., "Nature-Inspired Synthetic Oligourea Foldamer Channels Allow Water Transport With High Salt Rejection," *Chemistry* 9 (2023): 2237–2254, https://doi.org/10.1016/j.chempr.2023.04.007.

39. L.-B. Huang, A. Hardiagon, I. Kocsis, et al., "Hydroxy Channels–Adaptive Pathways for Selective Water Cluster Permeation," *Journal of the American Chemical Society* 143 (2021): 4224–4233, https://doi.org/10.1021/jacs.0c11952.

40. D. Mondal, B. R. Dandekar, M. Ahmad, A. Mondal, J. Mondal, and P. Talukdar, "Selective and Rapid Water Transportation Across a Self-Assembled Peptide-Diol Channel via the Formation of a Dual Water Array," *Chemical Science* 13 (2022): 9614–9623, https://doi.org/10.1039/D2SC01737G.

41. I. M. Andrei, A. Chaix, B. T. Benkhaled, et al., "Selective Water Pore Recognition and Transport Through Self-Assembled Alkyl-Ureido-Trianglamine Artificial Water Channels," *Journal of the American Chemical Society* 145 (2023): 21213–21221, https://doi.org/10.1021/jacs.3c02815.

42. A. Mondal, D. Mondal, S. Sarkar, U. Shivpuje, J. Mondal, and P. Talukdar, "Self-Assembled Hydrazide-Based Nanochannels: Efficient Water Translocation and Salt Rejection," *Angewandte Chemie International Edition* 64 (2025): e202415510, https://doi.org/10.1002/anie.202415510.

43. S. Farooq, J. A. Malla, M. Nedyalkova, et al., "Rapid Water Permeation by Aramid Foldamer Nanochannels With Hydrophobic Interiors," *Angewandte Chemie International Edition* 64 (2025): e202504170, https://doi.org/10.1002/anie.202504170.

44. S. Pophali, D.-D. Su, R. Ata, et al., "Metal-Directed Self-Assembly of Minimal Heterochiral Peptides Into Metallo-Supramolecular β-Helical Tubules for Artificial Transmembrane Water Channels," *Journal of the American Chemical Society* 147 (2025): 17404–17415, https://doi.org/10.1021/jacs.5c03970.

45. L.-B. Huang, D.-D. Su, A. Hardiagon, et al., "Water-Pore Flow Permeation Through Multivalent H-Bonding Pyridine-2,6-dicarboxamide-histamine/Histidine Water Channels," *Journal of the American Chemical Society* 147 (2025): 678–686, https://doi.org/10.1021/jacs.4c13072.

46. P. Wanjari, I. Stroia, A. van der Lee, M. Baaden, and M. Barboiu, "Dynamic Regulation of Proton and Water Transport Through an Acylhydrazone-Based Photoresponsive Channel," *Journal of the American Chemical Society* 147 (2025): 35264–35274, https://doi.org/10.1021/jacs.5c05942.

47. M. E. Halim, A. Bandyopadhyay, L. Sun, et al., "Synthesis of Bromo- and Iodo-Substituted Pyromellitic Diimide-Based [2+2]- and [3+3]Macrocycles, and Their Absorption Spectra and Electrochemical and Inclusion Properties," *Tetrahedron Letters* 56 (2015): 6970–6974, https://doi.org/10.1016/j.tetlet.2015.10.070.

48. Y. Wang, H. Wu, and J. F. Stoddart, "Molecular Triangles: A New Class of Macrocycles," *Accounts of Chemical Research* 54 (2021): 2027–2039, https://doi.org/10.1021/acs.accounts.1c00108.

49. S. Garain and F. Würthner, "Photofunctional Cyclophane Host–Guest Systems," *Chemical Communications* 61 (2025): 3081–3092, https://doi.org/10.1039/D4CC06070A.

50. R. R. Puniya, M. Chhapoliya, R. Singhal, and D. Singh, "Pyromellitic Diimides and Naphthalene Diimides: From Versatile Supramolecular Building Blocks to Advanced Materials," *Materials Today Advances* 28 (2025): 100627, https://doi.org/10.1016/j.mtadv.2025.100627.

51. Y. Zhao and D. G. Truhlar, "The M06 Suite of Density Functionals for Main Group Thermochemistry, Thermochemical Kinetics, Noncovalent Interactions, Excited States, and Transition Elements: Two New Functionals and Systematic Testing of Four M06-Class Functionals and 12 Other Functionals," *Theoretical Chemistry Accounts* 120 (2008): 215–241, https://doi.org/10.1007/s00214-007-0310-x.

52. D. Bassolino-Klimas, H. E. Alper, and T. R. Stouch, "Mechanism of Solute Diffusion Through Lipid Bilayer Membranes by Molecular Dynamics Simulation," *Journal of the American Chemical Society* 117 (1995): 4118–4129, https://doi.org/10.1021/ja00119a028.

53. M. Ozu, J. J. Alvear-Arias, M. Fernandez, et al., "Aquaporin Gating: A New Twist to Unravel Permeation Through Water Channels," *International Journal of Molecular Sciences* 23 (2022): 12317, https://doi.org/10.3390/ijms232012317.

54. X. Liu, J. Yang, H. Liu, X. Yuan, G. Liu, and S. Pu, "Pyromellitic Diimide-Based Luminophors: Tunable Aggregation-Induced Emission (AIE) and Reversible Mechanofluorochromism Characteristics," *Journal of Photochemistry and Photobiology A: Chemistry* 417 (2021): 113344, https://doi.org/10.1016/j.jphotochem.2021.113344.

55. C. L. Ren, X. Ding, A. Roy, et al., "A Halogen Bond-Mediated Highly Active Artificial Chloride Channel With High Anticancer Activity," *Chemical Science* 9 (2018): 4044–4051, https://doi.org/10.1039/C8SC00602D.

56. J. M. Wang, R. M. Wolf, J. W. Caldwell, P. A. Kollman, and D. A. Case, "Development and Testing of a General Amber Force Field," *Journal of Computational Chemistry* 25 (2004): 1157–1174, https://doi.org/10.1002/jcc.20035.

57. U. K. Eriksson, G. Fischer, R. Friemann, G. Enkavi, E. Tajkhorshid, and R. Neutze, "Subangstrom Resolution X-Ray Structure Details Aquaporin-Water Interactions," *Science* 340 (2013): 1346–1349, https://doi.org/10.1126/science.1234306.

Supporting Information

Additional supporting information can be found online in the Supporting Information section.

Supporting File 1: anie74121-sup-0001-SuppMat.pdf.

Supporting File 2: anie74121-sup-0002-MovieS1.avi.